On the Collective Importance of Model Physics and Data Assimilation on Mesoscale Convective System and Precipitation Forecasts over Complex Terrain

CHRISTOFORUS BAYU RISANTO,[a] JAMES M. MOKER JR.,[b] AVELINO F. ARELLANO JR.,[a] CHRISTOPHER L. CASTRO,[a] YOLANDE L. SERRA,[c] THANG M. LUONG,[d] AND DAVID K. ADAMS[e]

[a] *Department of Hydrology and Atmospheric Sciences, The University of Arizona, Tucson, Arizona*
[b] *56th Operations Support Squadron Weather Flight, Luke Air Force Base, Glendale, Arizona*
[c] *Cooperative Institute for Climate, Ocean, and Ecosystem Studies, University of Washington, Seattle, Washington*
[d] *Physical Science and Engineering Division, King Abdullah University of Science and Technology, Thuwal, Saudi Arabia*
[e] *Instituto de Ciencias de la Atmósfera y Cambio Climático, Universidad Nacional Autónoma de México, Mexico City, Mexico*

(Manuscript received 13 August 2022, in final form 8 May 2023, accepted 10 May 2023)

ABSTRACT: Forecasting mesoscale convective systems (MCSs) and precipitation over complex terrain is an ongoing challenge even for convective-permitting numerical models. Here, we show the value of combining mesoscale constraints to improve short-term MCS forecasts for two events during the North American monsoon season in 2013, including the following: 1) the initial specification of moisture, via GPS-precipitable water vapor (PWV) data assimilation (DA); 2) kinematics via modification of cumulus parameterization; and 3) microphysics via modification of cloud microphysics parameterization. A total of five convective-permitting Weather Research and Forecasting (WRF) Model experiments is conducted for each event to elucidate the impact of these constraints. Results show that combining GPS-PWV DA with a modified Kain–Fritsch scheme and double-moment microphysics provides relatively the best forecast of both North American monsoon MCSs and convective precipitation in terms of timing, location, and intensity relative to available precipitation and cloud-top temperature observations. Additional examination on the associated reflectivity, vertical wind field, equivalent potential temperature, and hydrometeor distribution of MCS events show the added value of each individual constraint to forecast performance.

SIGNIFICANCE STATEMENT: Forecasting thunderstorm clouds and rain over mountainous regions is challenging because of limitations in having radar and rain gauges and in resolving physical drivers in forecast models. We examine the value of considering all possible constraints by incorporating moisture into these models, and correcting physics in the model treatment of cumulus and cloud microphysics parameterizations. This study demonstrates that assimilating moisture and using modified Kain–Fritsch and double-moment microphysics schemes provides the best thunderstorm cloud and rain forecasts in terms of timing, location, and intensity. Each correction improves key properties of these storms such as vertical wind, along with distribution of water in various phases. We highlight the need to improve our efforts on effectively integrating these constraints into current and future forecasts.

KEYWORDS: Complex terrain; Cloud microphysics; Global positioning systems (GPS); Mesoscale forecasting; Convective parameterization; Data assimilation

1. Introduction

Accurate forecasting of mesoscale convective systems (MCSs; Houze 2012) is an important need in real-time numerical weather prediction (NWP) given their hydrometeorological significance (Schumacher and Rasmussen 2020). This is especially true for environments that are strongly influenced by complex orography, where resolving MCS interactions with physical processes is still challenging in current NWP models (e.g., Francis et al. 2021; Mulholland et al. 2019; Carrió et al. 2019). This limitation can be exacerbated by a lack of observational infrastructure, for example a ground-based radar network, which would provide useful constraints on these processes. Where such observations do exist, they can provide useful constraints to improve the physical representation and forecasting of MCSs, as has been demonstrated in the developed world, for example in Japan (e.g., Kawabata et al. 2013, 2014), the United States (e.g., Li et al. 2015; Degelia et al. 2019), and Europe (e.g., Stanesic and Brewster 2016). Additionally, the vertical sensitivity of space-based hydrometeorological measurements is insufficient to characterize the structure of the planetary boundary layer (e.g., Carroll et al. 2022; Nehrir et al. 2017), which is important for MCS maintenance and growth. In this paper, we examine the importance of considering the collective impact of model and observational constraints on NWP forecasts of MCSs in complex terrain in a subtropical environment.

Convection initiation, development, and organization have been known to be affected by multiple factors including surface orography at multiple scales (e.g., Doyle and Durran 2002; Nesbitt et al. 2008; Houze 2012; Wang et al. 2019; Ramos-Pérez et al. 2022; Rigo et al. 2022). Synoptic-scale winds are forcedly lifted by a mountain range and transport warm and humid air above (e.g., Boos and Pascale 2021).

Corresponding author: Christoforus Bayu Risanto, cbrisanto@arizona.edu

DOI: 10.1175/MWR-D-22-0221.1

Resultant increases in atmospheric instability, enhanced vertical shear, and flow perturbations can trigger secondary mesoscale circulations (e.g., slope and valley winds) downstream (Corsmeier et al. 2011; Grasmick and Geerts 2020; Grasmick et al. 2021). The cascading effect on mesoscale processes (kinematics, thermodynamic, and microphysics) leading to convective organization are intertwined and inseparable at these scales. Such influences on MCSs have been shown to be important, albeit separately in semiarid to arid regions with complex terrain including North and South America, Asia, and the Middle East. MCSs in the North American monsoon region in particular are initiated over the eastern slopes of the Sierra Madre Occidental (SMO) in the early afternoon and then propagate westward as the MCS matures along the western slopes of the SMO, finally dissipating over the Gulf of California by early evening (Nesbitt et al. 2008). Forecasts of convection initiation in the SMO are highly dependent on how accurately mesoscale environmental conditions, including land surface characteristics, are resolved (e.g., Ramos-Pérez et al. 2022).

One approach to improve convective precipitation forecasts in these regions is the use of convective-permitting modeling (CPM; ≤4-km horizontal grid spacing) to explicitly resolve convective organization at meso-γ scales (2–20 km; e.g., Prein et al. 2015; Freitas et al. 2020). In NWP applications, there may additionally be augmentation with a data assimilation (DA) system to improve representation of the initial hydrometeorological state (e.g., Gustafsson et al. 2018). However, for DA at CPM scales, some studies (e.g., Gong et al. 2023; Yang et al. 2020) have demonstrated the importance of a dense network of observations at least at meso-β scales (20–200 km), which is not typically available for purposes of real-time forecasting, as is the case in northwest Mexico. Retrospective simulations for the North American monsoon region using a convective-permitting configuration of the Advanced Research version of the Weather Research and Forecasting (WRF-ARW) model without DA (Moker et al. 2018) were shown to reasonably forecast North American monsoon MCSs but only for "strongly forced" cases, when the precipitation is strongly tied to synoptic-scale features such as the presence of inverted troughs. Such features are usually resolved in a coarser resolution model that would provide the lateral boundary forcing to the CPM, including the NCEP Global Forecast System or North American Mesoscale Forecast System. Convective-permitting WRF performed comparatively worse for "weakly forced" cases, for which moisture availability and atmospheric instability can be the more dominant drivers. However, the spatial and vertical distributions of these thermodynamic quantities may not be well resolved in convective-permitting WRF absent DA. An illustrative example is presented in Francis et al. (2021), where convective-permitting WRF failed to reproduce a MCS over the United Arab Emirates even when forced with several different NWP-based lateral boundary conditions. Francis et al. (2021) attributed the poor performance of their convective-permitting WRF forecasts to cloud microphysics and cumulus parameterization, which was intentionally activated in their 2.5-km domain, and an inadequate initial specification of moisture. To address the issue of the initial specification of moisture, Serra et al. (2016) and Moker et al. (2018) posited the potential utility of assimilating precipitable water vapor (PWV) retrieved from the Global Positioning System (GPS) network into convective-permitting NWP simulations. Subsequently, Risanto et al. (2021) implemented GPS-PWV DA into convective-permitting WRF for retrospective 2017 North American monsoon forecasts and did show improvements in at least the timing of precipitation although not in the spatial extent and intensity.

The challenge to skillfully forecast MCS-generated precipitation during the North American monsoon, even with the addition of GPS-PWV DA, highlights inadequacies in 1) the specification of initial conditions or 2) model physical parameterized processes in relation to the initiation and maintenance of convection. With respect to improving the physical representation of convection, one approach is to consider the meso-γ-scale (2–20 km) orographic effects on the modeled dynamic pressure within a modified cumulus parameterization. For example, Truong et al. (2009) originally modified the Kain–Fritsch convective scheme (mKF) to include the ratio between pressure perturbation and buoyant force in the diagnostic equation that computes updraft velocity, trigger function, and closure assumption (see details in the appendix). Its implementation over the Bach Ma Mountain region in Vietnam shows the reduction of modeled precipitation bias for a November 2004 extreme event by 87%, relative to the bias produced by the same model using the original Kain–Fritsch cumulus scheme. Note that the Kain–Fritsch (KF; Kain 2004) scheme does not explicitly account for the vertical pressure gradient and convective inhibition from the updraft surface layer to the lifted condensation level (Truong et al. 2009). The mKF was subsequently applied by Luong et al. (2018) over the North American monsoon region in hindcasting a convective precipitation event that occurred during the intensive observation period 2 (11–14 July 2004) of the North American Monsoon Experiment. That study showed that mKF generally produced a more realistic physical representation of development of MCSs and precipitation in the region using a nested grid configuration, including on an inner convective-permitting grid where the mKF was deactivated.

Improvements in the cloud microphysics parameterization may also increase the forecast skill of convective precipitation. For example, previous studies over the complex terrain of Idaho and Colorado by Grasmick et al. (2021) suggested that small-scale turbulence (Richardson number < 0.25) occurring in clouds increases vertical velocity, resulting in the growth of hydrometeors by collision and deposition with impacts on precipitation. The total ice water content under the turbulent region is 4 times greater than that under the nonturbulent region. Therefore, the choice of the model treatment of cloud microphysics is critical in representing MCS microphysical properties (e.g., Feng et al. 2018). Studying MCS organization over the Tibetan Plateau, Pu and Lin (2015) suggested that use of a double-moment scheme [e.g., WDM6 (Hong et al. 2010) or Morrison double moment (Morrison and Milbrandt 2011)] could generate a better MCS forecast in terms of cloud coverage than could a single-moment scheme

(e.g., WSM6; Hong and Lim 2006), although it does not necessarily improve the precipitation amount. The improvement is likely attributed to the calculation of both mixing ratios and number concentrations of the hydrometeors in the double-moment schemes. Using the Thompson double-moment microphysics, Grasmick et al. (2021) also has demonstrated agreements between modeled and observed snow growth.

Although we have highlighted studies showing different approaches to better simulate MCSs and improve forecast skill of convective precipitation over complex terrain, the findings from these studies have been inferred for only a particular model constraint considered in isolation. Incorporating multiple constraints on initial conditions and model physics may result in greater forecast skill than considering each constraint in isolation. As previously mentioned, the aim of this paper is to highlight the collective impact of multiple model constraints through a series of convective-permitting WRF forecast experiments. The specific constraints are as follows: 1) moisture correction, by assimilating GPS-PWV for atmospheric preconditioning at the initial forecast hour, 2) kinematic adjustment, by implementing either mKF or KF on intermediate, coarse model domains (>4-km horizontal grid spacing), and 3) microphysical complexity, by application of either the WSM6 or WDM6 schemes. We select two extreme precipitation cases occurring during the North American monsoon season, namely, 8 July 2013 representing the weakly forced days on which an inverted trough was absent and 9 July 2013 representing the strongly forced days on which an inverted trough was present in the North America monsoon core region (Higgins et al. 2006). Details of these events can be found in Moker et al. (2018). Experiments for these two cases provide insights on the impact of these mesoscale constraints for both synoptically strongly and weakly forced MCSs. This paper is structured as follows: First, we describe the datasets for assimilation and verification, and the methods for simulations and analyses in section 2. Results of this work are presented and discussed in section 3. We summarize our findings and their implications in section 4.

2. Data and methods

The GPS-PWV data used here was collected from the North American Monsoon GPS Transect Experiment 2013 (Transect 2013; Serra et al. 2016; Moker et al. 2018), where a network of GPS meteorological (GPS-Met) sensors was installed across northwest Mexico within the North American monsoon core region (Fig. 1b). This all-weather instrument retrieved the observed PWV at a 5-min interval from mid-June to mid-September 2013. See Serra et al. (2016) for details on the processing of the GPS data to retrieve the PWV signal for the Transect 2013 data.

We simulated the two cases utilizing the WRF-ARW (Skamarock et al. 2008; Powers et al. 2017), version 4.2. The model consists of three-nested domains with 30-, 10-, and 2.5-km grid spacing, respectively; and a hybrid sigma coordinate with 27 levels (Fig. 1a). It uses operational GFS forecast data with 0.5° resolution and updated every 6 h (https://www.ncei.noaa.gov/products/weather-climate-models/global-forecast) for the lateral boundary condition. The ensemble adjustment Kalman filter algorithm implemented in the Data Assimilation Research Testbed (DART; Anderson 2009) is coupled with the WRF-ARW. Detailed options of DART are listed in Table 1, similar to the options in Risanto et al. (2021).

For each simulation we conducted five experiments that consider the initial specification of moisture, specification of the convective updraft velocity per the KF and mKF schemes, and microphysical complexity. Following Risanto et al. (2021), each experiment (EXP) is initiated at 0000 UTC with perturbation to create 30 ensemble members, using the CV3 background error covariance option available in WRFDA (Barker et al. 2004) followed by a 6-h spinup. For EXP0, the spinup continues to 1800 UTC followed by an 18-h deterministic forecast using the ensemble mean at the 1800 UTC forecast with no DA (NODA). The WSM6 scheme is used with the KF scheme on domains 1 and 2 for this experiment. EXP1, our control run, is identical to EXP0 but uses mKF. For EXP2, EXP3, and EXP4, the forecast is preceded by 12 hourly cycles of assimilating GPS-PWV retrievals. A deterministic forecast is initiated at 1800 UTC using the ensemble mean of the final DA analyses with the following configuration: EXP2, EXP3, and EXP4 uses KF and WSM6, mKF and WSM6, and mKF and WDM6, respectively (see Table 2). The other physics schemes used in all the experiments are listed in Table 3.

For evaluation of the model forecast simulations, we examine the following variables and diagnostics: PWV, 10-m wind speed and direction (UV10), 2-m temperature (T2), 2-m dewpoint (Td2), liquid water path (LWP), 3-hourly total precipitation, cloud-top temperature (CTT), reflectivity, zonal wind U, vertical wind W, equivalent potential temperature θ_e, and hydrometeor mixing ratios. The modeled CTT representing the modeled MCS is verified by the Geostationary Operational Environmental Satellite Infrared (IR)/cloud-top temperature (hereinafter GOES-CTT) product with 4-km and 15-min resolution (https://www.ssec.wisc.edu/datacenter). For modeled precipitation verification, we use the Global Precipitation Measurement Final Precipitation V6 (GPMF; Huffman et al. 2018) with 0.1°- and 30-min resolution. Detailed discussion of the choice of precipitation ground reference can be found in Risanto et al. (2019).

We calculated the fractions skill score (FSS; Roberts 2008) for the modeled precipitation and CTT using a neighborhood-based verification technique that considers both the CTT and precipitation events within ±1 grid points (9 grid points in total) of GPMF, GOES-CTT, and convective-permitting WRF. We use the adjusted hourly precipitation thresholds (Risanto et al. 2021) based on 30-mm total daily precipitation. The CTT threshold is set to −40°C (233.15 K), which is within the MCS CTT range of Maddox (1980). For this comparison, the modeled precipitation and CTT are scaled up from 2.5-km horizontal resolution to the GPMF and GOES-CTT spatial resolutions, respectively, using the Earth System Modeling Framework "conserve" function within the National Center for Atmospheric Research (NCAR) Command Language (NCL), as used in Risanto et al. (2021). The FSS is represented in percentages.

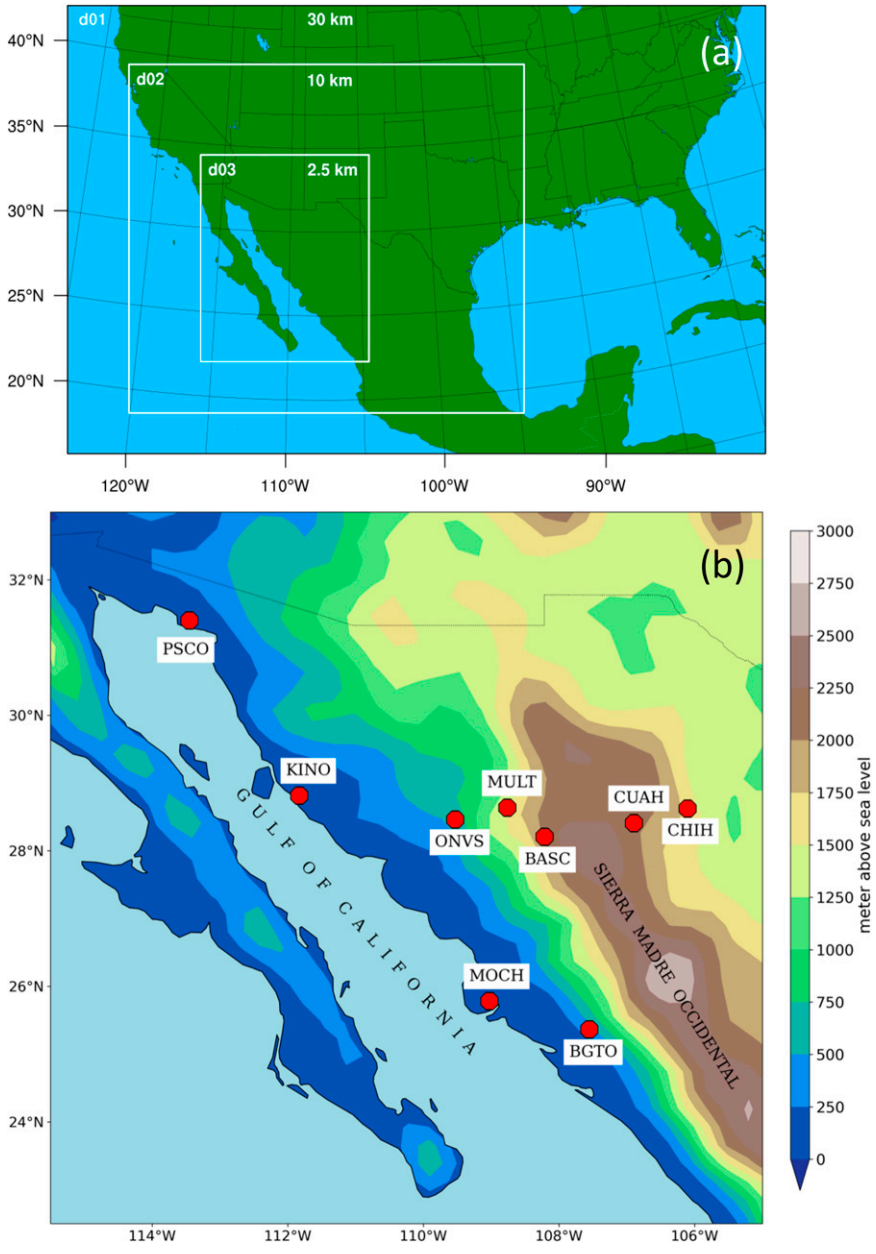

FIG. 1. (a) The Advanced Research version of the Weather Research and Forecasting (WRF-ARW) nested domain configuration. (b) The inner domain with nine Global Positioning System meteorological (GPS-met) sites of the Transect 2013. One of the sites (RAYN), not plotted in the figure, failed in mid-July and was excluded from the data assimilation. The elevation is shaded from 0 to 3000 m above sea level.

3. Results and discussion

Below, we present the results of the five experiments for the weakly forced MCS on 8 July 2013, as this was the case where MCS-generated precipitation is relatively more challenging to forecast per Moker et al. (2018) and thus of greater interest. In addition, we also discuss the results for the strongly forced MCS on 9 July 2013 as its corresponding figures are presented in this section.

a. Atmospheric preconditioning

Figure 2 shows a comparison of key state and diagnostic variables between EXP2 (DA) and EXP0 (NODA) to examine the impact of assimilating PWV for the KF-WSM6 WRF configuration. Difference plots highlight the response of convective-permitting WRF to adjustments made by DA across 12 cycles of hourly GPS-PWV assimilation prior to 1800 UTC. Consistent with our previous study of Risanto et al. (2021), the

TABLE 1. DART options. The WRF state fields being updated are *U*, *V*, *W*, PH, *T*, MU, QVAPOR, QCLOUD, QRAIN, QICE, QSNOW, U10, V10, T2, TH2, Q2, and PSFC. No observation outlier threshold rejection was done.

Parameter	Value
Filter type	Ensemble adjustment Kalman filter
Adaptive inflation	2—initial 1.0, 0.6 (initial mean, std dev)
Adaptive localization threshold	Disabled
Localization type	Gaspari–Cohn (Gaspari and Cohn 1999)
Horizontal localization half-width	445.97 km
Vertical localization half-width	3.5 km
Ensemble members	30
Sampling error correction	False
Assimilation interval	1 h

PWV in the domain for EXP2 is reduced up to 10 mm when compared with the EXP0 PWV at 1800 UTC (Figs. 2a,g), similar to the strongly forced day (Figs. 3a,g). This is especially the case over the northwestern portion of the domain where the GPS-PWV data (albeit still sparse) constrain the initial states of the convective-permitting WRF forecast (Figs. 2a and 3a). More notably, EXP2 also reduces the 10-m wind speed at 1800 UTC over the same region, as well as over the Gulf of California (Figs. 2b,h). This reduction also appears in the strongly forced day, when an increase in PWV west of the Gulf of California is observed (Figs. 3a,b,g,h). The decrease in 10-m wind speed and PWV suggests reduced low-level moisture advection (e.g., Jana et al. 2018).

The impact of GPS-PWV DA on the initial conditions also impacts the atmospheric thermodynamic fields in later forecasts. We show in Figs. 2c and 2i (cf. Figs. 3c,i) that the 3-hourly EXP2 Td2 (0000–0300 UTC) is higher than the EXP0 over the east side of the SMO and near the northern Gulf of California, indicating increased moisture near the surface as advected by the easterly and southeasterly winds, respectively. This is consistent with previous studies (e.g., Adams and Comrie 1997; Nesbitt et al. 2008; Mejia et al. 2010; Pascale and Bordoni 2016; Serra et al. 2016; Boos and Pascale 2021), which demonstrated westward and northwestward moisture advection over the region. This period also corresponds to the time of MCS initiation. Note that there is a reduction in Td2 over the northwest portion of the domain in EXP2 relative to EXP0 (Figs. 2c,i). In the same period

TABLE 2. The moisture, dynamical, and microphysical setups for each experiment (EXP).

	NODA	DA	KF	mKF	WSM6	WDM6
EXP0	✓		✓		✓	
EXP1	✓			✓	✓	
EXP2		✓	✓		✓	
EXP3		✓		✓	✓	
EXP4		✓		✓		✓

TABLE 3. The physics schemes that are used in each experiment (EXP) and applied to all domains.

WRF setting	Option chosen
Longwave radiation scheme	Rapid Radiative Transfer Model (Iacono et al. 2008)
Shortwave radiation scheme	Goddard (Chou and Suarez 1999)
Land surface scheme	Unified Noah (Tewari et al. 2004)
Planetary boundary layer scheme	Yonsei University (Hong and Lim 2006)

(Figs. 2d,j), the overall EXP2 T2 is higher than the EXP0 over the domain. This increase in T2 is even more pronounced on the strongly forced day (Figs. 3d,j). This lower EXP2 Td2 and warmer EXP2 T2 over the northwest portion of the domain (also found on the strongly forced day) is likely due to earlier precipitation in EXP0 (2300–0100 UTC) than in EXP2 (0300–0600 UTC), which increases dewpoint and lowers temperature near the surface in EXP0. Observational studies (e.g., Rigo et al. 2022) have found potential temperature decreases after the passing of thunderstorms over complex terrain.

The impact of GPS-PWV DA on 3-hourly mean LWP forecasts over the 0300–0600 UTC and 0600–0900 UTC periods, respectively, are shown in Figs. 2e, 2k, 2f, and 2l (Figs. 3e,k,f,l). These two periods correspond to the time of MCS development. It is very clear that the EXP2 forecast in the 0300–0600 UTC generates higher values of LWP over the SMO and lower values to the south than the EXP0 forecast. This still holds true but with smaller differences in the 0600–0900 UTC period. It appears that the EXP2 forecast impacts the production of liquid hydrometeors in the region, whereas the EXP0 forecast does not show a similar LWP even in the earlier hours when EXP0 precipitation occurs. The PWV correction in the initial forecast appears to be important and agrees with Kim and Kim (2022), who found that the underestimated LWP forecast of an MCS over Svalbard on 17/18 September 2017 is corrected by 0.036 kg m^{-2} at 0600 UTC 18 September when DA adjusted the PWV initial condition.

In summary, the results of EXP0 and EXP2 are consistent with our previous GPS-PWV DA study, where moisture-based DA adjustments in convective-permitting WRF result in atmospheric preconditioning (not only moisture) at the initial forecast hour. This most notably affects convection initiation and organization in the later forecast hours as reflected in Td2, T2, and LWP, regardless of the degree of synoptic forcing to the MCS.

b. *Precipitation and MCS coverage*

Consistent with Adams and Comrie (1997) and Nesbitt et al. (2008), the MCSs in all EXPs develop over the SMO eastern slopes at ~2100–0000 UTC, mature as they cross over the SMO at ~0100–0600 UTC, and propagate westward toward the Gulf of California (not shown) where they dissipate around 0900–1200 UTC. The exception is the EXP0 and EXP1 MCS, whose precipitation begins to dissipate at 0300 UTC (not shown). Figure 4 shows snapshots of 3-hourly total precipitation and hourly CTT for the MCS in EXP1, EXP2, EXP3, and

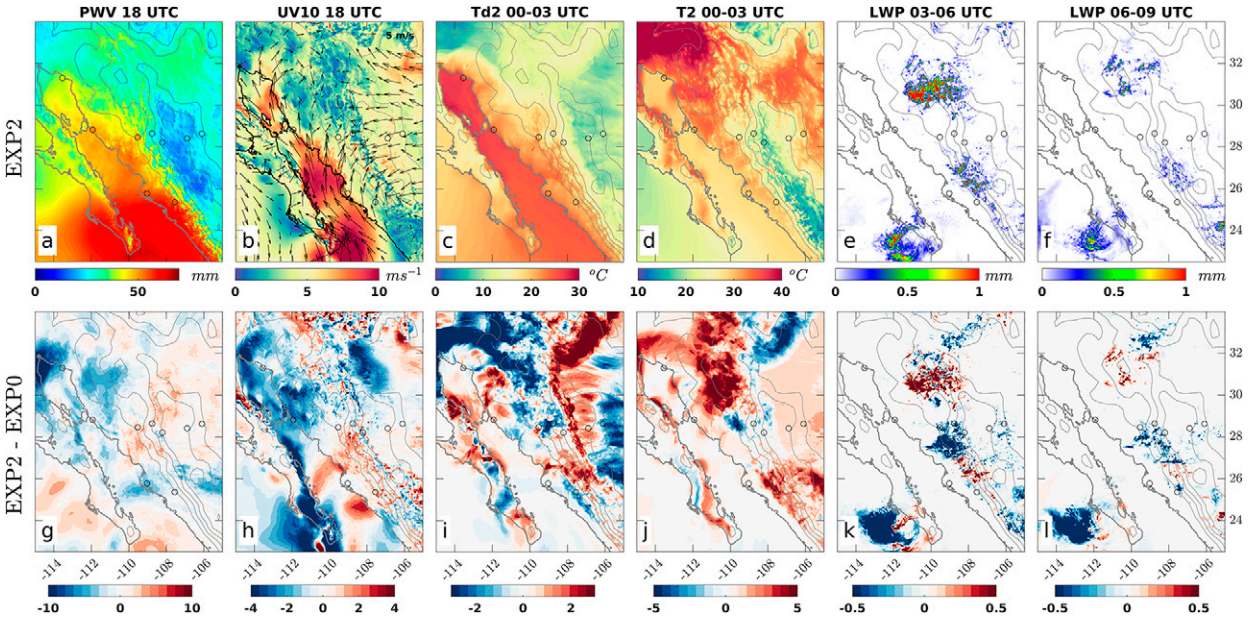

FIG. 2. Model response of GPS-PWV DA (1800 UTC; the analysis results) to atmospheric preconditioning (0000–0300 UTC) and development (0300–0900 UTC) of a weakly forced MCS over the North American monsoon region on the 8 Jul 2013 event: (a)–(f) the EXP2 PWV (with circles representing the GPS-PWV at each site color coded with values of the color bar), UV10, Td2, T2, and LWP, respectively. (g)–(l) The EXP2 difference of each variable relative to the EXP0 variables. Note that Td2, T2, and LWP are plotted as a 3-hourly average.

EXP4, along with GPMF precipitation and GOES-CTT. EXP1 (Figs. 4b,l), which uses mKF and no GPS-PWV DA, does not appear to generate precipitation intensity and coverage as well as EXP2 (Figs. 4c,m), which uses KF and includes GPS-PWV DA, at 0300–0600 UTC or 0600–0900 UTC. In particular, the EXP1 MCS at 0600 UTC (Fig. 4g) is not as organized as that of EXP2 (Fig. 4h). At 0900 UTC, the EXP1 MCS (Fig. 4q) has dissipated whereas the EXP2 MCS (Fig. 4r) retains its spatial extent. The FSS difference between EXP1 and EXP2 is about 2.1% and 0.7% for the 0300–0600 UTC and 0600–0900 UTC precipitation totals, respectively, while the FSS difference of their CTT is about 2.2% at 0600 UTC and 23.4% at 0900 UTC.

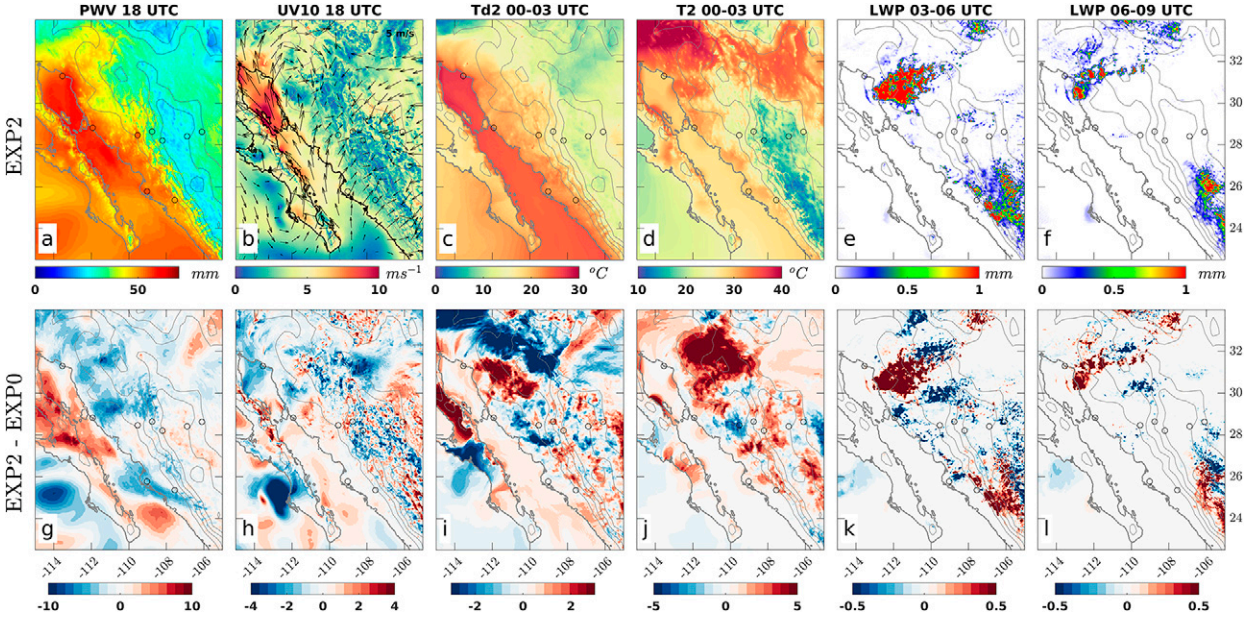

FIG. 3. As in Fig. 2, but for the 9 Jul 2013 strongly forced day.

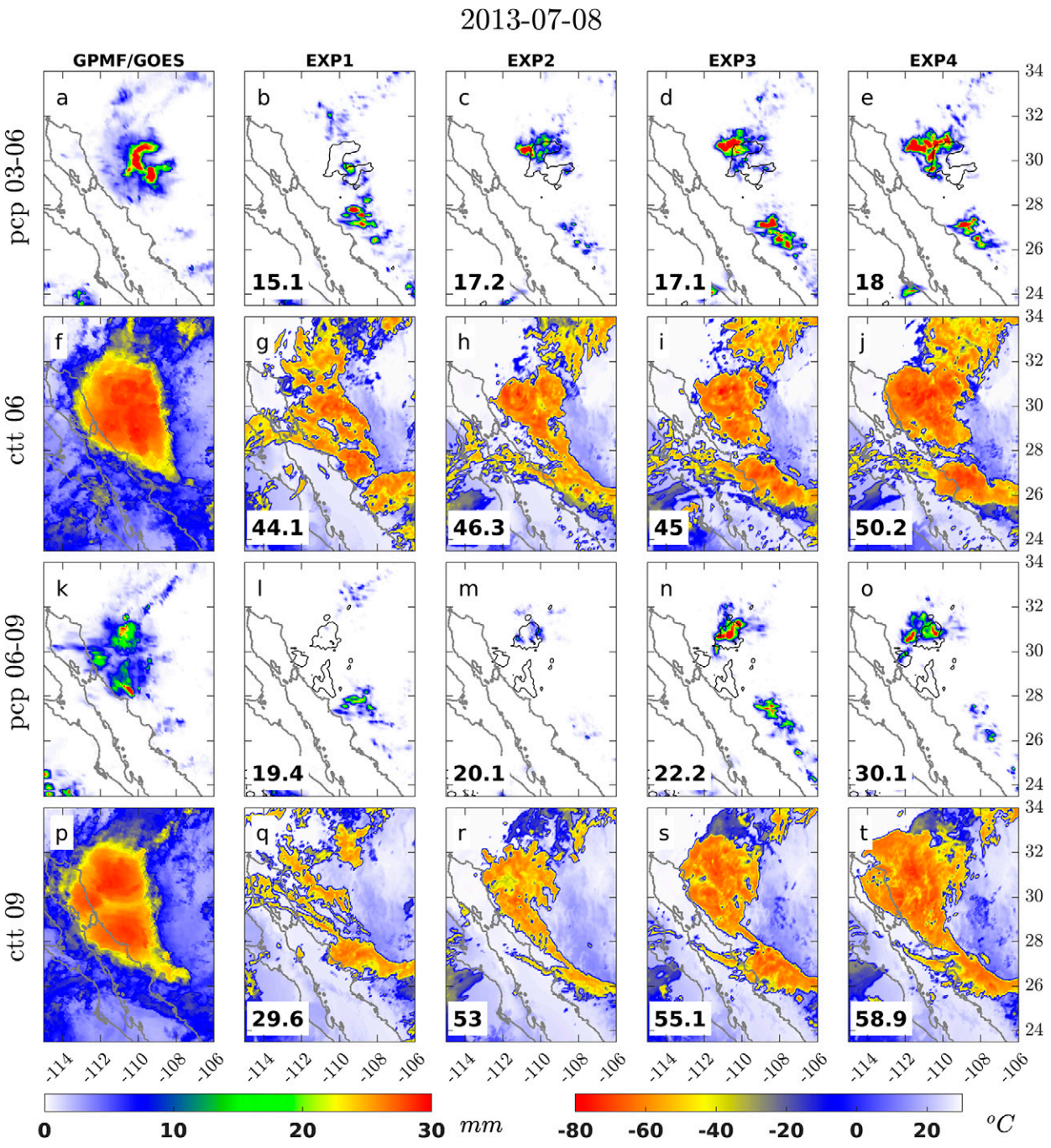

FIG. 4. Comparison of observed precipitation (pcp) from GPMF and cloud-top temperatures from GEOS-CTT with WRF forecasts initialized at 1800 UTC 8 Jul 2013 of a weakly forced MCS developing at 0300–0900 UTC 9 Jul 2013 (9–15 h into the forecast). The value at the bottom of most panels corresponds to the fractions skill score (FSS; Roberts 2008) of the precipitation and CTT forecasts as evaluated against the observations. The FSS unit is in percentages. The isohyet in each modeled precipitation panel is set to 10 mm.

For the strongly forced day, EXP2 (Figs. 5c,h,m,r) shows higher FSS in CTT and precipitation than EXP1 (Figs. 5b,g,l,q) except in 0300–0600 UTC. There is only a small difference between EXP1 and EXP0 (not shown) suggesting that mKF alone is not effective at improving precipitation forecasts, whereas GPS-PWV DA (even with just limited GPS-PWV) provides a useful constraint. These results are consistent with previous GPS-PWV DA studies on MCSs in other regions with complex terrain (e.g., Seko et al. 2011; Oigawa et al. 2018; Yang et al. 2020).

The combination of mKF and GPS-PWV DA (EXP3) shows evidence that their collective impact is even greater

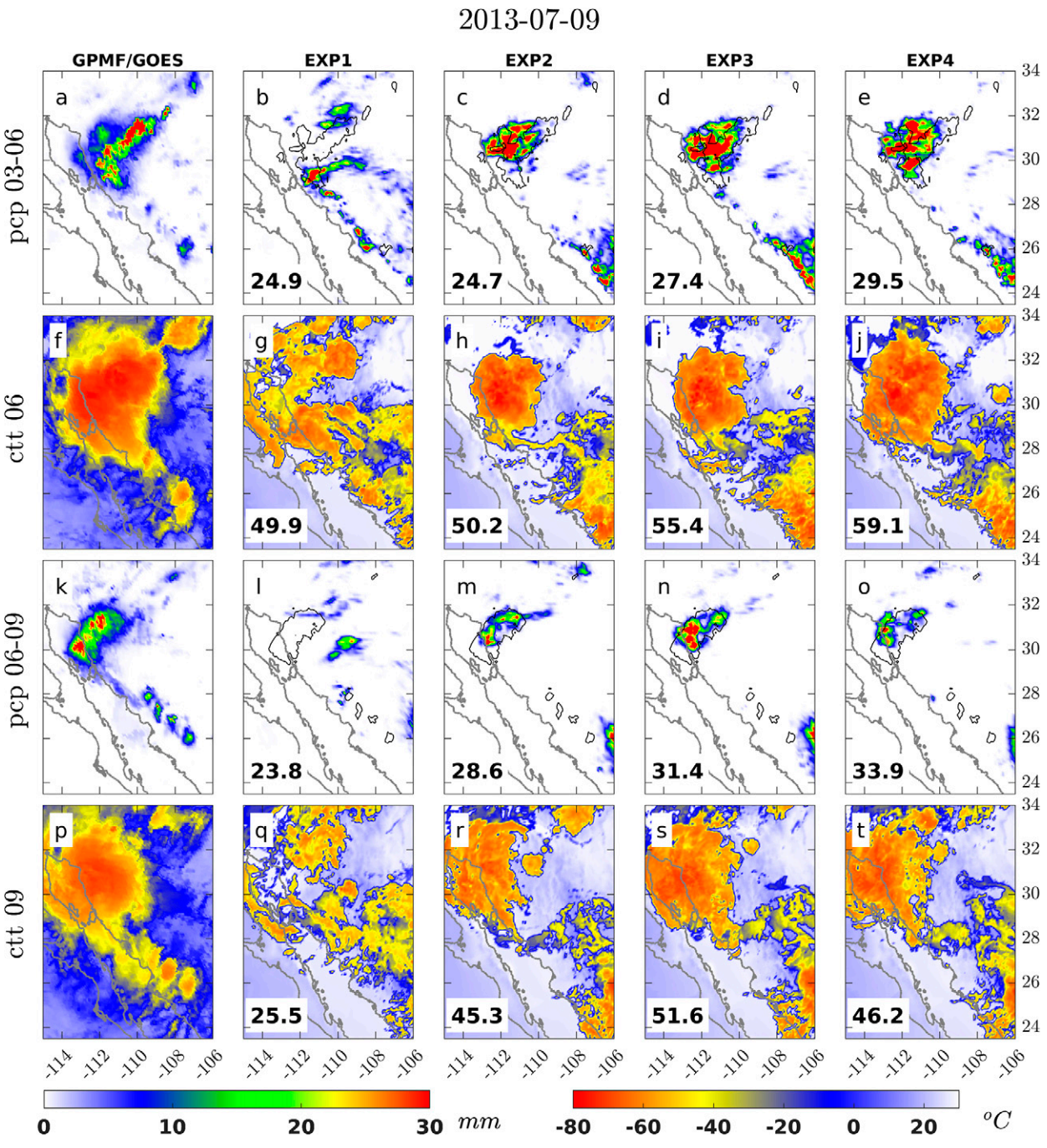

FIG. 5. As in Fig. 4, but for the 9 Jul 2013 strongly forced day.

than that of GPS-PWV DA alone (EXP2). In Fig. 4d, EXP3 0300–0600 UTC precipitation in the weakly forced day appears to cover a larger area and has higher intensity than EXP2, even though the FSS of EXP3 precipitation is lower than EXP2. The relatively low score is likely due to overestimation of precipitation between 26° and 28°N. However, the 0600–0900 UTC precipitation in EXP3 (Fig. 4n) lingers, while EXP2 precipitation coverage is now fairly low. For this period, the FSS of EXP3 precipitation is about 2.1% higher than that of EXP2 (2.8% for strongly forced day in Figs. 5m,n). Consistent with precipitation, the EXP3 MCS (Fig. 4i) appears to have greater coverage than that of EXP2 at 0600 UTC even though the FSS of the EXP3 CTT is lower. The collective impact is clearly seen at 0900 UTC when EXP3 MCS coverage (Fig. 4s) is similar to the MCS observed by GOES-CTT and is larger than EXP2 (Fig. 4r). The FSS of EXP3 CTT is about 2% higher than EXP2 (6.3% for strongly forced MCS in Figs. 5r,s). These results suggest that combining GPS-PWV DA and mKF extends the precipitation

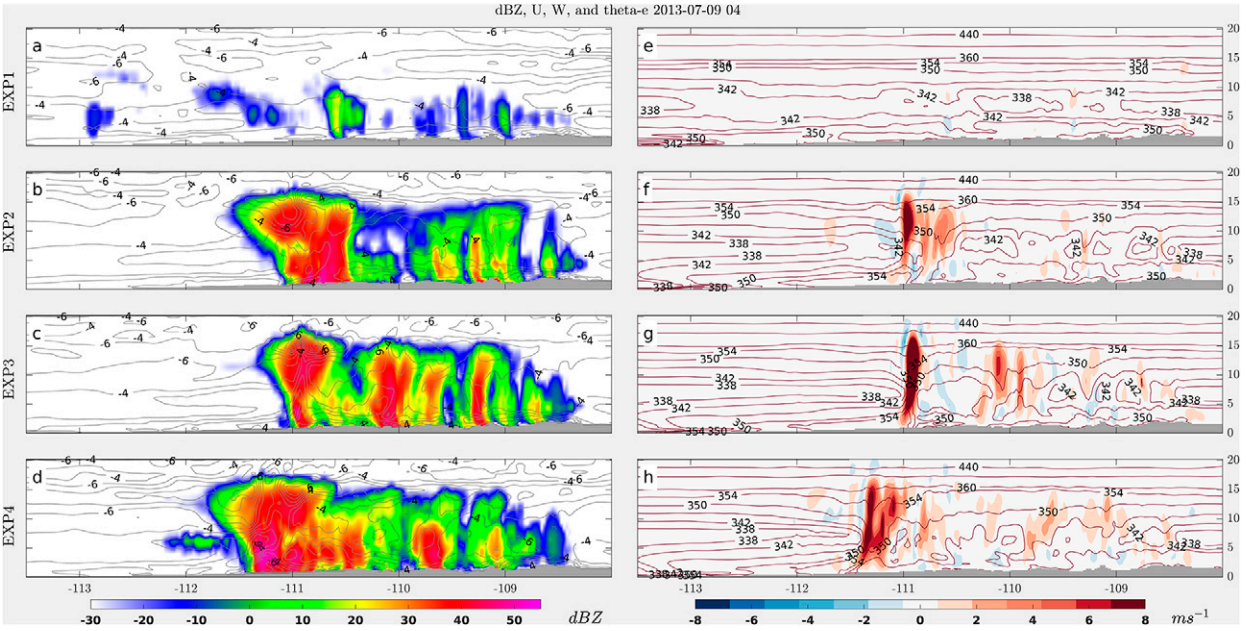

FIG. 6. (a)–(d) Vertical profiles of reflectivity (dBZ) superimposed with isotach of zonal wind (m s^{-1}), and (e)–(h) the vertical wind (m s^{-1}) superimposed with isotherm of equivalent potential temperature θ_e (K) along the longitudinal cross section of 30.4°–30.6°N of the weakly forced MCS simulation coinciding with its initiation at 0400 UTC 9 Jul 2013.

occurrence and maintains MCS size beyond 0600 UTC even though it does not significantly improve the precipitation or MCS coverage for the 0300–0600 UTC forecast. Our results for EXP3 precipitation agree with Luong et al. (2018), in which the bias of the modeled 24-h precipitation generated by mKF over the SMO was reduced by up to 25 mm in comparison with KF. Yet, this improvement does not happen for our convective-permitting WRF simulation (Fig. 4d) when only the cumulus parameterization is modified. It is likely that the presence of inverted through matters as the simulation in Luong et al. (2018) was for a strongly forced day in agreement with our results shown in Figs. 5d and 5n.

We show the collective impact of GPS-PWV DA, mKF, and cloud microphysics (WDM6) in EXP4 (Figs. 4e,j,o,t). The spatial extent of EXP4 precipitation for 0300–0600 UTC is similar to GPMF. The precipitation FSS is 18% (29.5% for strongly forced day in Fig. 5e) when evaluated against the GPMF, and better than any other EXPs. EXP4 also continues convective precipitation into 0600–0900 UTC (Fig. 4o), with better spatial coverage than EXP3. Its FSS is 7.9% higher than EXP3, clearly due to low precipitation bias between 26° and 28°N in EXP4. When compared with the other EXPs, the MCS coverage and CTT resemble that of GOES-CTT at both 0600 and 0900 UTC (Figs. 4j,t). The CTT FSSs are 5.2% and 3.8% higher at 0600 and 0900 UTC, respectively, than EXP3. These results suggest that using the WDM6 microphysical scheme in convective-permitting WRF in combination with moisture-based constraints on the specification of initial conditions (GPS-PWV DA) and mKF improves the forecast precipitation timing and coverage, as well as forecast MCS timing, coverage, and CTT. The results hold true (but not as significant) for the strongly forced simulation (Figs. 5j,t) even though it is associated with an inverted through, a dynamical constraint that makes the atmosphere synoptically favorable for MCS organization (e.g., Bieda et al. 2009; Seastrand et al. 2015; Lahmers et al. 2016).

c. *MCS and atmospheric vertical profile*

To support our model-data comparison across experiments in the previous section, we present two model diagnostics of the simulated MCSs. We show in Fig. 6 (and Fig. 7) the vertical profile of reflectivity (dBZ), U (m s^{-1}), W (m s^{-1}), and θ_e (K) forecasts along a longitudinal cross section of the MCS over 30.4°–30.6°N coinciding with the convection initiation around 0400 UTC from EXP2, EXP3, and EXP4. This is meant to demonstrate the response of the convective-permitting WRF to the combination of constraints in the vertical distribution of moisture, temperature, and wind.

The peak reflectivity in EXP1 (mKF; no GPS-PWV DA) occurs earlier at ~2300–0100 UTC (not shown) as precipitation occurs, but it does not exceed 40 dBZ, which is a typical threshold for convective cores (e.g., Houze 2012). The EXP1 W peaks around 2300 UTC with wind speed greater than 6 m s^{-1} at 10 km MSL (not shown). By 0400 UTC, the EXP1 reflectivity and W have dissipated (Figs. 6a,e and 7a,e) and the atmosphere is stable as the θ_e increases with height. In EXP2 (Figs. 6b,f), the MCS structure exhibits high reflectivity (>40 dBZ) between 111.0° and 110.5°W with westward U and a region of strong W (>6 m s^{-1}) extends from approximately 8 to 15 km MSL with θ_e decreasing with height (indicating instability) around 111.0°W. Again, the significant difference between EXP1 and EXP2 is attributed to the GPS-PWV constraint in EXP2's initial condition. By using mKF with GPS-PWV DA,

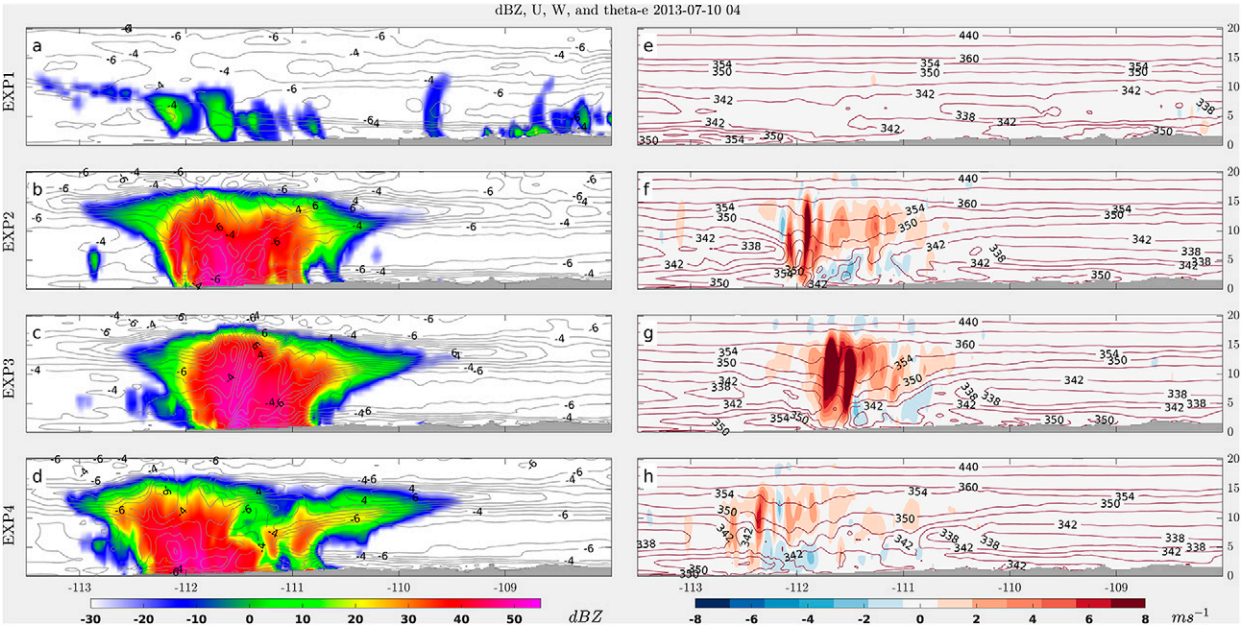

FIG. 7. As in Fig. 6, but for the 9 Jul 2013 strongly forced day.

EXP3 (Fig. 6g) expands the MCS structure with high reflectivity (around 50 dBZ) from 111° to 109°W. EXP3 also generates strong instability indicated by its θ_e decreasing with height and a W field greater than 6 m s^{-1} between 2 and 16 km MSL over 111°W (Fig. 6g) that is significantly larger than EXP2. The difference between EXP2 and EXP3 shows the impact of explicitly calculating vertical pressure gradients in the mKF scheme (Luong et al. 2018; Truong et al. 2009). Note that the strongly forced MCS in EXP2 and EXP3 (Figs. 7b,c) are well formed as compared with its weakly forced counterpart.

Consistent with the results in section 3b, EXP4 (Fig. 6d) has a larger MCS structure and larger high reflectivity (>40 dBZ) area than EXP2 and EXP3, with the MCS coverage expanding to 111.5°W and westward U. The area of high W is not as well-defined in EXP3, but EXP4 (Fig. 6h) has a more expansive wind field with wind speeds greater than 6 m s^{-1} between 111° and 111.5°W from 2 to 16 km MSL, which is dynamically and physically consistent with the larger MCS reflectivity at 0400 UTC for this experiment. Its decreased θ_e with height around the 111.5°W also indicates the presence of strong instability. High W (>6 m s^{-1}) increases the cloud hydrometeor number and growth due to condensation and deposition (e.g., Grasmick et al. 2021) and contributes to cloud expansion (e.g., Judt and Chen 2014) and cloud vertical structure (e.g., Houze 2012, 2018). EXP4 demonstrates that the WDM6 microphysical scheme, in combination with GPS-PWV DA and the use of the mKF scheme, impacts the W distribution and magnitude and the extent of the MCS as shown by the high reflectivity area regardless of the degree of synoptic forcing.

d. Hydrometeor mixing ratio

In Figs. 8 and 9 we evaluate the mean concentration of solid and liquid hydrometeors along the cross section from 0300 to 0900 UTC generated by each EXP. These include mixing ratios of cloud (QCLOUD), rain (QRAIN), ice (QICE), graupel (QGRAUP), and snow (QSNOW). We find that there is little difference in hydrometeor concentration between EXP0 and EXP1. Both concentrations peak about 200 g kg^{-1} at 2300 UTC (not shown) and then dissipate to almost zero by 0300 UTC.

In EXP2 (Fig. 8b), the peak concentration, mostly graupel and snow, is located at 10 km MSL. This is likely the impact of GPS-PWV DA in the initial condition (1800 UTC), as precipitation is also extended beyond 0300 UTC. When applying mKF (EXP3; Fig. 8c), the peak concentrations increase by about 100 g kg^{-1} at 10 km MSL relative to EXP2. The liquid hydrometeors (QCLOUD and QRAIN) appear to increase as well, but not as significantly (<100 g kg^{-1}). This increase is consistent with our precipitation comparison in section 3b. The hydrometeor concentrations also appear to be affected by the explicit vertical pressure gradient calculation over the complex terrain (EXP3 versus EXP2).

EXP4 (Fig. 8d) exhibits high concentrations of all hydrometeors with its peak located at around 9 km MSL. The increase is mostly due to QGRAUP and QSNOW, with total concentrations > 400 g kg^{-1}. The QCLOUD and QRAIN also increase for this EXP, especially at and below 5 km MSL. Note that EXP4 has QRAIN down to 1 km MSL, below that of the other EXPs (Fig. 8d). This is due to the propagation of convective precipitation reaching a much lower elevation near the Gulf of California in the later forecast hours. Grant et al. (2022) shows a linear relationship ($R^2 > 0.6$) between vertical velocity and conversion rates of water vapor to condensed water in deep convection. The results shown in Fig. 8d clearly demonstrate that the WDM6 scheme in combination with GPS-PWV DA and the mKF scheme impacts the distribution

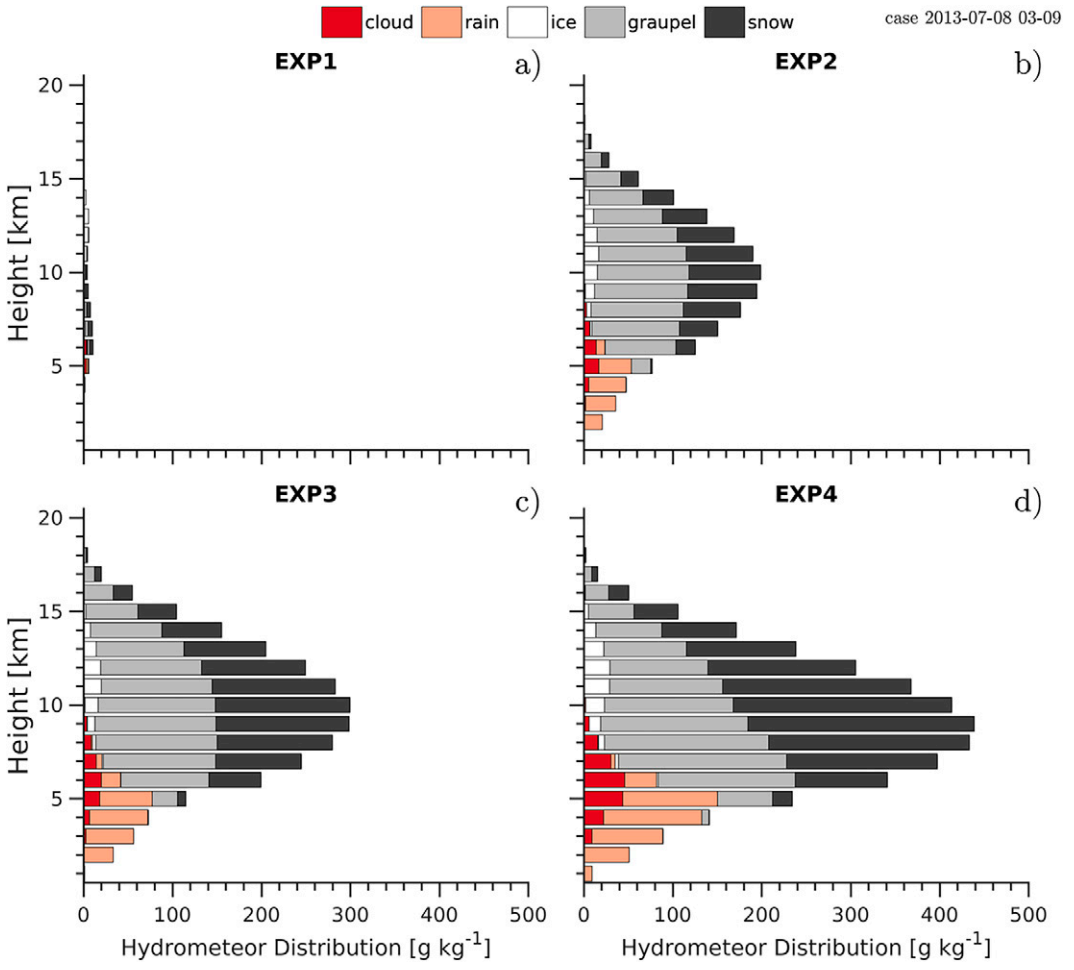

FIG. 8. (a)–(d) Mean WRF forecasts of hydrometeor mixing ratios [g H_2O (kg air)$^{-1}$] during a weakly forced MCS averaged across the longitude cross section shown in Fig. 6 and period of its development (from 0300 to 0900 UTC 9 Jul 2013). Shades correspond to liquid (QCLOUD and QRAIN) and solid (QICE, QGRAUP, and QSNOW) hydrometeors. Note that EXP4 [(d)] contains the most hydrometeors.

of hydrometeor mixing ratios at all levels at the later forecast hours, consistent with EXP4 precipitation results discussed in section 3b and with Grant et al. (2022). On the other hand, WDM6 reduces the magnitude for the strongly forced day (Fig. 9d) consistent with its reduction in modeled precipitation spatial extent for 0600–0900 UTC (Fig. 5o). This is likely due to a shift in the balance between dynamical and microphysical processes in an already strongly forced MCS.

4. Summary and implications

This study investigates the collective impact of moisture, physical, and microphysical constraints on North American monsoon MCS and convective precipitation forecasts over the SMO using a convective-permitting WRF model. Past studies have demonstrated the challenges of forecasting MCSs and precipitation over complex terrain due to lack of observations, lack of accuracy in the NWP model dynamics and thermodynamics, and limited capability of the single-moment microphysical schemes that are typically used for real-time forecasting. We conduct a series of experiments to elucidate the collective impact (in contrast to individual impact) of model constraints in the form of: 1) moisture (GPS-PWV) data assimilation (DA vs no DA), 2) modified cumulus parameterization (KF vs mKF), and 3) addition of number concentration in the cloud microphysics parameterization (WSM6 vs WDM6) on the skill of a deterministic forecast of MCSs and precipitation over complex terrain. Two North American monsoon precipitation events representing weakly and strongly forced days with respect to the synoptic forcing are examined to further demonstrate the impacts of GPS-PWV DA and cumulus and microphysical parameterizations. Our results show that EXP4, which combines all three mesoscale constraints—that is, GPS-PWV DA, mKF, and WDM6—provides the best forecast of North American monsoon MCS and precipitation coverage over the SMO in terms of timing, location, and intensity, as indicated by the MCS and precipitation FSS values relative to available observations.

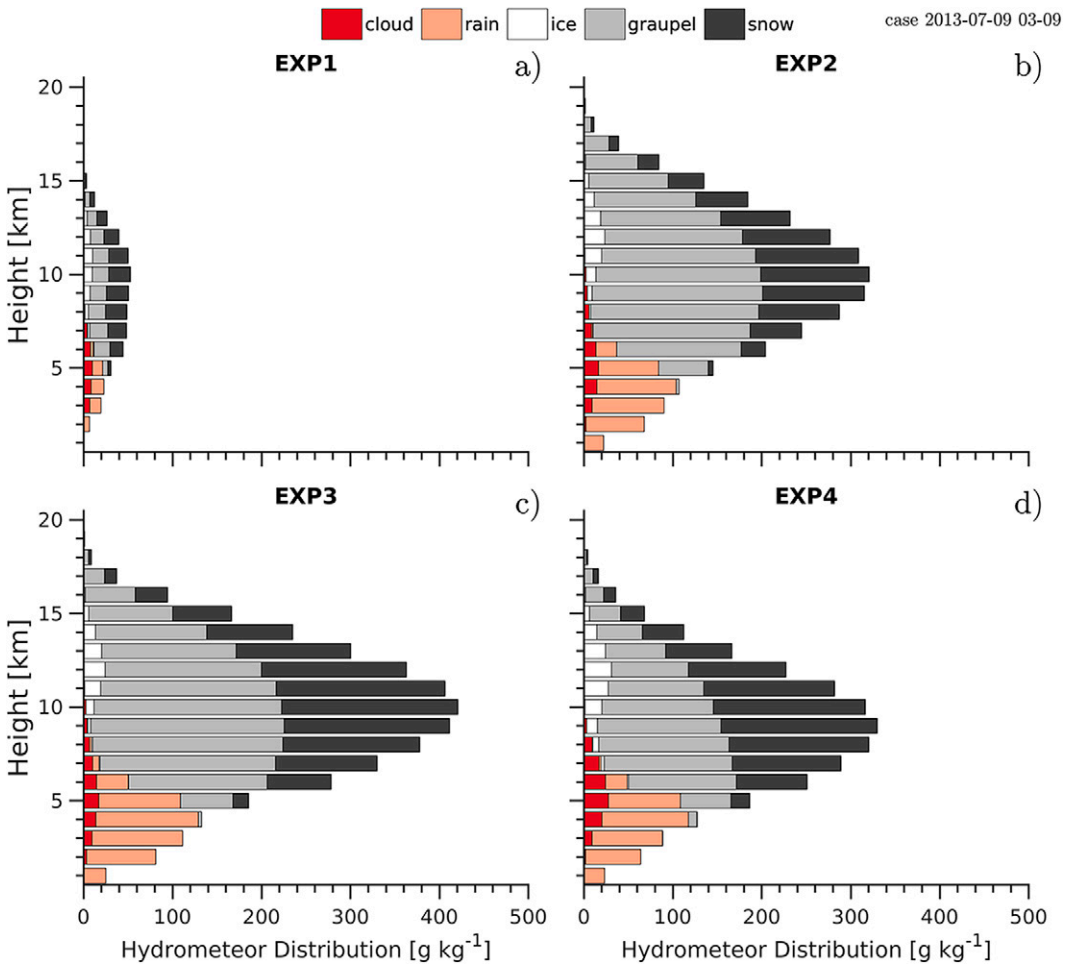

FIG. 9. As in Fig. 8, but for the 9 Jul 2013 strongly forced day. Note that EXP3 [(c)] contains the most hydrometeors.

While the combination of all three factors provides the best forecast, each constraint adds value to convective-permitting WRF performance, as seen by examining MCS morphology in terms of reflectivity and hydrometeor distribution for EXP1, EXP2, EXP3, and EXP4.

While this study provides evidence of the collective impact of these constraints, it should also be emphasized that there are important limitations to this study. First, we acknowledge that the present study is limited in the number of cases examined. The strongly and weakly forced days are both extreme cases with clear mature MCS cloud shields visible in the GOES IR imagery. Considering the impacts of these constraints on the forecast of MCS structure and precipitation representation under these opposing synoptic conditions, we expect that implementing the constraints will yield improved results more generally. Future work will include the 22 strongly and 40 weakly forced days that have been identified by Moker et al. (2018) to improve the statistical characterization of forecast improvement.

Second, while the assimilation of the GPS-PWV has substantially reduced the moisture bias in the region, there are associated uncertainties in the DA system, notably with regard to covariance inflation and localization. Due to limitations in the number of GPS-Met sites as installing and maintaining GPS-Met sensors in the SMO is physically challenging, the assimilation of the GPS-PWV strongly depends on the background error covariance and the choice of horizontal and vertical localizations (Pu et al. 2013; Gustafsson et al. 2018). The heterogeneous surface representation of complex terrain resulting in multiscale turbulence and thermal fluxes is also limited by the model horizontal and vertical resolutions (e.g., Hacker et al. 2018). DA systems such as ensemble Kalman filter (EnKF) would generally reject observed data with relatively large departure from the forecast data due to terrain elevation mismatch. This could degrade the analysis.

Third, even though the modified convective scheme has improved modeled precipitation and MCS over complex terrain (e.g., Truong et al. 2009; Luong et al. 2018), further testing of this scheme is still needed as our results confirmed the finding of Luong et al. (2018). We suggest future studies should evaluate the use of mKF in other regions characterized with complex terrain and a similar climatic regime as that of the North American monsoon region to broaden our understanding of

the physical processes in deep convection initiation and growth as well as precipitation.

Fourth, the MCS and precipitation forecasts in our convective-permitting WRF appear to be sensitive to microphysical schemes, which is consistent with Freitas et al. (2020) who demonstrate the significant contribution of microphysical schemes to total precipitation in convective-permitting NWP models, relative to convective schemes. Our results also agree with Pu and Lin (2015) where WDM6 helps the model to reproduce better forecasts of MCS cloud coverage than single-moment schemes. Implementing double-moment microphysics schemes in NWP models increases run time by at least 20% relative to a single moment (Jeworrek et al. 2021). Some studies (e.g., Conrick and Mass 2019; Jeworrek et al. 2021) have demonstrated that double-moment schemes are not needed to produce good forecasts of precipitation with more than 1-day accumulation, but microphysical schemes that count more parameters (e.g., mixing ratios and concentrations) seems to matter in subdaily precipitation forecasts over complex terrain like the SMO, as our results show.

These findings clearly highlight the need to consider both constraints in initial conditions and specification of model parameterizations to improve our understanding and predictive capability of MCSs in complex terrain. This is particularly the case in these regions where even basic observational infrastructure is lacking. Our findings support past and ongoing efforts that highlight the need to improve observational and modeling capabilities, and also consider appropriately and effectively the collective multiscale constraints on MCS processes. These are usually intertwined (e.g., Majumdar et al. 2021), as well as accounting for known coupling and feedbacks of these processes, including aerosol-meteorology and land-atmosphere interactions (e.g., Zhang et al. 2021). Reducing uncertainties in MCS prediction is particularly relevant and timely in light of observed and projected changes in climate conditions, which have corresponding expected changes to MCSs in the future (Schumacher and Rasmussen 2020; Chang et al. 2015).

Acknowledgments. This work is supported by Binational Consortium of Regional Scientific Development and Innovation at The University of Arizona and the Consejo Nacional de Ciencia y Tecnología de México. Yoland L. Serra's contributions to this work were funded by U.S. National Science Foundation Grant AGS-1261226. We thank Modhi Ali Alshammari and Chayan Roychaudury for reading and giving feedback on the paper. We also thank the editor and the reviewers for their comments that improved our paper. The authors declare that there is no conflict of interest.

Data availability statement. This study used NCL, MATLAB, and Python to analyze the simulation output and create the figures. The observation and simulation data are stored on the computer clusters of the Department of Hydrology and Atmospheric Science at The University of Arizona and are available upon request.

APPENDIX

Modified Kain–Fritsch Convective Scheme

The ratio between pressure perturbation and buoyant force (PDB; Truong et al. 2009) introduced in the diagnostic equations in the modified Kain–Fritsch (mKF) convective scheme can be calculated as follows:

$$\mathrm{PDB} = \frac{\theta_{v,0}\dfrac{\partial(\overline{\pi} - \pi_0)}{\partial z}}{g\left[\dfrac{T_u - T_0}{T_0} - \dfrac{\overline{p} - p_0}{p_0}\left(1 - \dfrac{C_v}{C_p}\right)\right]}.$$

In the numerator, $\theta_{v,0}$ and z are the virtual potential temperature (K) and the height (m), respectively; and π is the Exner function. In the denominator, g is gravity, T is temperature, and p is pressure. The subscripts 0 and u are the synoptic-scale variable and updraft variable, respectively, and the overbar indicates the grid scale variable. The C_v and C_p are the heat capacities at constant volume and constant pressure, respectively. The Exner function is defined by

$$\pi = C_p(p/p_{00})^{R_d/C_p},$$

where p_{00} is 1000 hPa and R_d is the gas constant for dry air. By adding this ratio into the original KF diagnostic equation, the updraft velocity is redefined as

$$\frac{1}{2}\frac{dw_u^2}{dz} = g\left(\frac{T_u - \overline{T}}{\overline{T}}\right)(1 + \mathrm{PDB}) - \mathrm{Ent} - P_{\mathrm{drag}},$$

where w is the updraft velocity, Ent is entrainment, and P_{drag} is the effect of drag from solid and liquid substances, the trigger function is redefined as

$$F_{\mathrm{tri}} = g\frac{T_u(z) - \overline{T}(z)}{\overline{T}(z)}[1 + \mathrm{PDB}(z)],$$

and the convective available potential energy (CAPE) that is used for the closure assumption is redefined as

$$\mathrm{CAPE} = \int_{\mathrm{LCL}}^{\mathrm{CT}} g\frac{T_u(z) - \overline{T}(z)}{\overline{T}(z)}[1 + \mathrm{PDB}(z)]\,dz,$$

where CT is cloud-top height (m) and LCL is the height of the lifting condensation level (m). With these modified diagnostic equations, deep convection can be maintained as long as the vertical gradient of pressure perturbation is adequately large and positive (Truong et al. 2009).

REFERENCES

Adams, D. K., and A. C. Comrie, 1997: The North American monsoon. *Bull. Amer. Meteor. Soc.*, **78**, 2197–2214, https://doi.org/10.1175/1520-0477(1997)078<2197:TNAM>2.0.CO;2.

Anderson, J. L., 2009: Spatially and temporally varying adaptive covariance inflation for ensemble filters. *Tellus*, **61A**, 72–83, https://doi.org/10.1111/j.1600-0870.2008.00361.x.

Barker, D. M., W. Huang, Y.-R. Guo, A. J. Bourgeois, and Q. N. Xiao, 2004: A three-dimensional variational data assimilation system for MM5: Implementation and initial results. *Mon. Wea. Rev.*, **132**, 897–914, https://doi.org/10.1175/1520-0493(2004)132%3C0897:ATVDAS%3E2.0.CO;2.

Bieda, S. W., III, C. L. Castro, S. L. Mullen, A. C. Comrie, and E. Pytlak, 2009: The relationship of transient upper-level troughs to variability of the North American monsoon system. *J. Climate*, **22**, 4213–4227, https://doi.org/10.1175/2009JCLI2487.1.

Boos, W. R., and S. Pascale, 2021: Mechanical forcing of the North American monsoon by orography. *Nature*, **599**, 611–615, https://doi.org/10.1038/s41586-021-03978-2.

Carrió, D. S., V. Homar, and D. M. Wheatley, 2019: Potential of an EnKF storm-scale data assimilation system over sparse observation regions with complex orography. *Atmos. Res.*, **216**, 186–206, https://doi.org/10.1016/j.atmosres.2018.10.004.

Carroll, B. J., A. R. Nehrir, S. A. Kooi, J. E. Collins, R. A. Barton-Grimley, A. Notari, D. B. Harper, and J. Lee, 2022: Differential absorption lidar measurements of water vapor by the High-Altitude Lidar Observatory (HALO): Retrieval framework and first results. *Atmos. Meas. Tech.*, **15**, 605–626, https://doi.org/10.5194/amt-15-605-2022.

Chang, H.-I., C. L. Castro, C. M. Carrillo, and F. Dominguez, 2015: The more extreme nature of U.S. warm season climate in the recent observational record and two "well-performing" dynamically downscaled CMIP3 models. *J. Geophys. Res. Atmos.*, **120**, 8244–8263, https://doi.org/10.1002/2015JD023333.

Chou, M.-D., and M. J. Suarez, 1999: A solar radiation parameterization for atmospheric studies. Tech. Memo. NASA/TM-1999-104606, Vol. 15, 38 pp.

Conrick, R., and C. F. Mass, 2019: An evaluation of simulated precipitation characteristics during OLYMPEX. *J. Hydrometeor.*, **20**, 1147–1164, https://doi.org/10.1175/JHM-D-18-0144.1.

Corsmeier, U., and Coauthors, 2011: Processes driving deep convection over complex terrain: A multi-scale analysis of observations from COPS IOP 9c. *Quart. J. Roy. Meteor. Soc.*, **137**, 137–155, https://doi.org/10.1002/qj.754.

Degelia, S. K., X. Wang, and D. J. Stensrud, 2019: An evaluation of the impact of assimilating AERI retrievals, kinematic profilers, rawinsondes, and surface observations on a forecast of a nocturnal convection initiation event during the PECAN field campaign. *Mon. Wea. Rev.*, **147**, 2739–2764, https://doi.org/10.1175/MWR-D-18-0423.1.

Doyle, J. D., and D. R. Durran, 2002: The dynamics of mountain-wave-induced rotors. *J. Atmos. Sci.*, **59**, 186–201, https://doi.org/10.1175/1520-0469(2002)059<0186:TDOMWI>2.0.CO;2.

Feng, Z., L. R. Leung, R. A. Houze Jr., S. Hagos, J. Hardin, Q. Yang, B. Han, and J. Fan, 2018: Structure and evolution of mesoscale convective systems: Sensitivity to cloud microphysics in convection-permitting simulations over the United States. *J. Adv. Model. Earth Syst.*, **10**, 1470–1494, https://doi.org/10.1029/2018MS001305.

Francis, D., M. Temimi, R. Fonesca, N. R. Nelli, R. Abida, M. Weston, and Y. Whebe, 2021: On the analysis of a summertime convective event in a hyperarid environment. *Quart. J. Roy. Meteor. Soc.*, **147**, 501–525, https://doi.org/10.1002/qj.3930.

Freitas, S. R., W. M. Putnam, N. P. Arnold, D. K. Adams, and G. A. Grell, 2020: Cascading toward a kilometer-scale GCM: Impacts of a scale-aware convection parameterization in the Goddard Earth Observing System GCM. *Geophys. Res. Lett.*, **47**, e2020GL087682, https://doi.org/10.1029/2020GL087682.

Gaspari, G., and S. E. Cohn, 1999: Construction of correlation functions in two and three dimensions. *Quart. J. Roy. Meteor. Soc.*, **125**, 723–757, https://doi.org/10.1002/qj.49712555417.

Gong, Y., Z. Liu, P. W. Chan, and K. K. Hon, 2023: Assimilating GNSS PWV and radiosonde meteorological profiles to improve the PWV and rainfall forecasting performance from the Weather Research and Forecasting (WRF) model over South China. *Atmos. Res.*, **286**, 106677, https://doi.org/10.1016/j.atmosres.2023.106677.

Grant, L. D., S. C. van den Heever, Z. S. Haddad, J. Bukowski, P. J. Marinescu, R. L. Storer, D. J. Posselt, and G. L. Stephens, 2022: A linear relationship between vertical velocity and condensation processes in deep convection. *J. Atmos. Sci.*, **79**, 449–466, https://doi.org/10.1175/JAS-D-21-0035.1.

Grasmick, C., and B. Geerts, 2020: Detailed dual-Doppler structure of Kelvin–Helmholtz waves from an airborne profiling radar over complex terrain. Part I: Dynamic structure. *J. Atmos. Sci.*, **77**, 1761–1782, https://doi.org/10.1175/JAS-D-19-0108.1.

——, ——, X. Chu, J. R. French, and R. M. Rauber, 2021: Detailed dual-Doppler structure of Kelvin–Helmholtz waves from an airborne profiling radar over complex terrain. Part II: Evidence for precipitation enhancement from observations and modeling. *J. Atmos. Sci.*, **78**, 3455–3472, https://doi.org/10.1175/JAS-D-20-0392.1.

Gustafsson, N., and Coauthors, 2018: Survey of data assimilation methods for convective-scale numerical weather prediction at operational centres. *Quart. J. Roy. Meteor. Soc.*, **144**, 1218–1256, https://doi.org/10.1002/qj.3179.

Hacker, J., C. Draper, and L. Madaus, 2018: Challenges and opportunities for data assimilation in mountainous environments. *Atmosphere*, **9**, 127, https://doi.org/10.3390/atmos9040127.

Higgins, W., and Coauthors, 2006: The NAME 2004 field campaign and modeling strategy. *Bull. Amer. Meteor. Soc.*, **87**, 79–94, https://doi.org/10.1175/BAMS-87-1-79.

Hong, S.-Y., and J.-O. J. Lim, 2006: The WRF single-moment 6-class microphysics scheme (WSM6). *J. Korean Meteor. Soc.*, **42**, 129–151.

——, K.-S. S. Lim, Y.-H. Lee, J.-C. Ha, H.-W. Kim, S.-J. Ham, and J. Dudhia, 2010: Evaluation of the WRF double-moment 6-class microphysics scheme for precipitating convection. *Adv. Meteor.*, **2010**, 707253, https://doi.org/10.1155/2010/707253.

Houze, R. A., Jr., 2012: Orographic effects on precipitating clouds. *Rev. Geophys.*, **50**, RG1001, https://doi.org/10.1029/2011RG000365.

——, 2018: 100 years of research on mesoscale convective systems. *A Century of Progress in Atmospheric and Related Sciences: Celebrating the American Meteorological Society Centennial*, *Meteor. Monogr.*, No. 59, Amer. Meteor. Soc., https://doi.org/10.1175/AMSMONOGRAPHS-D-18-0001.1.

Huffman, G. J., and Coauthors, 2018: NASA Global Precipitation Measurement (GPM) Integrated Multi-SatellitE Retrievals for GPM (IMERG). Algorithm Theoretical Basis Doc., version 5.2, 35 pp., https://gpm.nasa.gov/sites/default/files/document_files/IMERG_ATBD_V5.2_0.pdf.

Iacono, M. J., J. S. Delamere, E. J. Mlawer, M. W. Shephard, S. A. Clough, and W. D. Collins, 2008: Radiative forcing by long-lived greenhouse gases: Calculations with the AER radiative transfer models. *J. Geophys. Res.*, **113**, D13103, https://doi.org/10.1029/2008JD009944.

Jana, S., B. Rajagopalan, M. A. Alexander, and A. J. Ray, 2018: Understanding the dominant sources and tracks of moisture for summer rainfall in the southwest United States. *J.*

Geophys. Res. Atmos., **123**, 4850–4870, https://doi.org/10.1029/2017JD027652.

Jeworrek, J., G. West, and R. Stull, 2021: WRF precipitation performance and predictability for systematically varied parameterizations over complex terrain. *Wea. Forecasting*, **36**, 893–913, https://doi.org/10.1175/WAF-D-20-0195.1.

Judt, F., and S. S. Chen, 2014: An explosive convective cloud system and its environmental conditions in MJO initiation observed during DYNAMO. *J. Geophys. Res. Atmos.*, **119**, 2781–2795, https://doi.org/10.1002/2013JD021048.

Kain, J. S., 2004: The Kain–Fritsch convective parameterization: An update. *J. Appl. Meteor.*, **43**, 170–181, https://doi.org/10.1175/1520-0450(2004)043<0170:TKCPAU>2.0.CO;2.

Kawabata, T., Y. Shoji, H. Seko, and K. Saito, 2013: A numerical study on a mesoscale convective system over a subtropical island with 4D-Var assimilation of GPS slant total delays. *J. Meteor. Soc. Japan*, **91**, 705–721, https://doi.org/10.2151/jmsj.2013-510.

——, H. Iwai, H. Seko, Y. Shoji, K. Saito, S. Ishii, and K. Mizutani, 2014: Cloud-resolving 4D-Var assimilation of Doppler wind lidar data on a meso-gamma-scale convective system. *Mon. Wea. Rev.*, **142**, 4484–4498, https://doi.org/10.1175/MWR-D-13-00362.1.

Kim, D.-H., and H. M. Kim, 2022: Effect of data assimilation on the polar WRF with 3DVAR on the prediction of radiation, heat flux, cloud, and near surface atmospheric variables over Svalbard. *Atmos. Res.*, **272**, 106155, https://doi.org/10.1016/j.atmosres.2022.106155.

Lahmers, T. M., C. L. Castro, D. K. Adams, Y. L. Serra, J. J. Brost, and T. Luong, 2016: Long-term changes in the climatology of transient inverted troughs over the North American monsoon region and their effects on precipitation. *J. Climate*, **29**, 6037–6064, https://doi.org/10.1175/JCLI-D-15-0726.1.

Li, Z., S. Feng, Y. Liu, W. Lin, M. Zhang, T. Toto, A. M. Vogelmann, and S. Endo, 2015: Development of fine-resolution analyses and expanded large-scale forcing properties: 1. Methodology and evaluation. *J. Geophys. Res. Atmos.*, **120**, 654–666, https://doi.org/10.1002/2014JD022245.

Luong, T. M., C. L. Castro, T. M. Nguyen, W. W. Cassell, and H.-I. Chang, 2018: Improvement in the modeled representation of North American monsoon precipitation using a modified Kain–Fritsch convective parameterization scheme. *Atmosphere*, **9**, 31, https://doi.org/10.3390/atmos9010031.

Maddox, R. A., 1980: Mesoscale convective complexes. *Bull. Amer. Meteor. Soc.*, **61**, 1374–1387, https://doi.org/10.1175/1520-0477(1980)061<1374:MCC>2.0.CO;2.

Majumdar, S. J., and Coauthors, 2021: Multiscale forecasting of high-impact weather: Current status and future challenges. *Bull. Amer. Meteor. Soc.*, **102**, E635–E659, https://doi.org/10.1175/BAMS-D-20-0111.1.

Mejia, J. F., M. W. Douglas, and P. J. Lamb, 2010: Aircraft observations of the 12–15 July 2004 moisture surge event during the North American Monsoon Experiment. *Mon. Wea. Rev.*, **138**, 3498–3513, https://doi.org/10.1175/2010MWR3228.1.

Moker, J. M., Jr., C. L. Castro, A. F. Arellano Jr., Y. L. Serra, and D. K. Adams, 2018: Convective-permitting hindcast simulations during the North American monsoon GPS transect experiment 2013: Establishing baseline model performance without data assimilation. *J. Appl. Meteor. Climatol.*, **57**, 1683–1710, https://doi.org/10.1175/JAMC-D-17-0136.1.

Morrison, H., and J. Milbrandt, 2011: Comparison of two-moment bulk microphysics schemes in idealized supercell thunderstorm simulations. *Mon. Wea. Rev.*, **139**, 1103–1130, https://doi.org/10.1175/2010MWR3433.1.

Mulholland, J. P., S. W. Nesbitt, and R. J. Trapp, 2019: A case study of terrain influences on upscale convective growth of a supercell. *Mon. Wea. Rev.*, **147**, 4305–4324, https://doi.org/10.1175/MWR-D-19-0099.1.

Nehrir, A. R., and Coauthors, 2017: Emerging technologies and synergies for airborne and space-based measurements of water vapor profiles. *Surv. Geophys.*, **38**, 1445–1482, https://doi.org/10.1007/s10712-017-9448-9.

Nesbitt, S. W., D. J. Gochis, and T. J. Lang, 2008: The diurnal cycle of clouds and precipitation along the Sierra Madre Occidental observed during NAME-2004: Implications for warm season precipitation estimation in complex terrain. *J. Hydrometeor.*, **9**, 728–743, https://doi.org/10.1175/2008JHM939.1.

Oigawa, M., T. Tsuda, H. Seko, Y. Shoji, and E. Realini, 2018: Data assimilation experiment of precipitable water vapor observed by a hyper-dense GNSS receiver network using a nested NHM-LETKF system. *Earth Planets Space*, **70**, 74, https://doi.org/10.1186/s40623-018-0851-3.

Pascale, S., and S. Bordoni, 2016: Tropical and extratropical controls of Gulf of California surges and summertime precipitation over the southwestern United States. *Mon. Wea. Rev.*, **144**, 2695–2718, https://doi.org/10.1175/MWR-D-15-0429.1.

Powers, J. G., and Coauthors, 2017: The Weather Research and Forecasting Model: Overview, system efforts, and future directions. *Bull. Amer. Meteor. Soc.*, **98**, 1717–1737, https://doi.org/10.1175/BAMS-D-15-00308.1.

Prein, A. F., and Coauthors, 2015: A review on regional convection-permitting climate modeling: Demonstrations, prospects, and challenges. *Rev. Geophys.*, **53**, 323–361, https://doi.org/10.1002/2014RG000475.

Pu, Z., and C. Lin, 2015: Evaluation of double-moment representation of ice hydrometeors in bulk microphysical parameterization: Comparison between WRF numerical simulations and UND-citation data during MC3E. *Geosci. Lett.*, **2**, 11, https://doi.org/10.1186/s40562-015-0028-x.

——, H. Zhang, and J. Anderson, 2013: Ensemble Kalman filter assimilation of near-surface observations over complex terrain: Comparison with 3DVAR for short-range forecasts. *Tellus*, **65A**, 19620, https://doi.org/10.3402/tellusa.v65i0.19620.

Ramos-Pérez, O., D. K. Adams, C. A. Ochoa-Moya, and A. I. Quintanar, 2022: A climatology of mesoscale convective systems in northwest Mexico during the North American monsoon. *Atmosphere*, **13**, 665, https://doi.org/10.3390/atmos13050665.

Rigo, T., O. Rodríguez, J. Bech, and C. Farnell, 2022: An observational analysis of two companion supercell storms over complex terrain. *Atmos. Res.*, **272**, 106149, https://doi.org/10.1016/j.atmosres.2022.106149.

Risanto, C. B., C. L. Castro, J. M. Moker Jr., A. F. Arellano Jr., D. K. Adams, L. M. Fierro, and C. M. Minjarez Sosa, 2019: Evaluating forecast skills of moisture from convective-permitting WRF-ARW model during 2017 North American monsoon season. *Atmosphere*, **10**, 694, https://doi.org/10.3390/atmos10110694.

——, ——, A. F. Arellano Jr., J. M. Moker Jr., and D. K. Adams, 2021: The impact of assimilating GPS precipitable water vapor in convective-permitting WRF-ARW on North American monsoon precipitation forecasts over Northwest Mexico. *Mon. Wea. Rev.*, **149**, 3013–3035, https://doi.org/10.1175/MWR-D-20-0394.1.

Roberts, N., 2008: Assessing the spatial and temporal variation in the skill of precipitation forecasts from an NWP model. *Meteor. Appl.*, **15**, 163–169, https://doi.org/10.1002/met.57.

Schumacher, R. S., and K. L. Rasmussen, 2020: The formation, character and changing nature of mesoscale convective systems. *Nat. Rev. Earth Environ.*, **1**, 300–314, https://doi.org/10.1038/s43017-020-0057-7.

Seastrand, S., Y. Serra, C. Castro, and E. Ritchie, 2015: The dominant synoptic-scale modes of North American monsoon precipitation. *Int. J. Climatol.*, **35**, 2019–2032, https://doi.org/10.1002/joc.4104.

Seko, H., T. Miyoshi, Y. Shoji, and K. Saito, 2011: Data assimilation experiments of precipitable water vapour using the LETKF system: Intense rainfall event over Japan 28 July 2008. *Tellus*, **63A**, 402–414, https://doi.org/10.1111/j.1600-0870.2010.00508.x.

Serra, Y. L., and Coauthors, 2016: The North American Monsoon GPS Transect Experiment 2013. *Bull. Amer. Meteor. Soc.*, **97**, 2103–2115, https://doi.org/10.1175/BAMS-D-14-00250.1.

Skamarock, W. C., and Coauthors, 2008: A description of the Advanced Research WRF version 3. NCAR Tech. Note NCAR/TN-475+STR, 113 pp., https://doi.org/10.5065/D68S4MVH.

Stanesic, A., and K. A. Brewster, 2016: Impact of radar data assimilation on the numerical simulation of a severe storm in Croatia. *Meteor. Z.*, **25**, 37–53, https://doi.org/10.1127/metz/2015/0574.

Tewari, M., and Coauthors, 2004: Implementation and verification of the unified Noah land surface model in the WRF model. *20th Conf. on Weather Analysis and Forecasting/16th Conf. on Numerical Weather Prediction*, Seattle, WA, Amer. Meteor. Soc., 14.2A, https://ams.confex.com/ams/pdfpapers/69061.pdf.

Truong, N. M., T. T. Tien, R. A. Pielke Sr., C. L. Castro, and G. Leoncini, 2009: A modified Kain–Fritsch scheme and its application for the simulation of an extreme precipitation event in Vietnam. *Mon. Wea. Rev.*, **137**, 766–789, https://doi.org/10.1175/2008MWR2434.1.

Wang, C., D. Wu, and F. Zhang, 2019: Modification of the convective adjustment time-scale in the Kain–Fritsch eta scheme for the case of weakly forced deep convection over the Tibetan Plateau region. *Quart. J. Roy. Meteor. Soc.*, **145**, 1915–1932, https://doi.org/10.1002/qj.3535.

Yang, S.-C., Z.-M. Huang, C.-Y. Huang, C.-C. Tsai, and T.-K. Yeh, 2020: A case study on the impact of ensemble data assimilation with GNSS-Zenith total delay and radar data on heavy rainfall prediction. *Mon. Wea. Rev.*, **148**, 1075–1098, https://doi.org/10.1175/MWR-D-18-0418.1.

Zhang, Y., J. Fan, Z. Li, and D. Rosenfeld, 2021: Impacts of cloud microphysics parameterizations on simulated aerosol–cloud interactions for deep convective clouds over Houston. *Atmos. Chem. Phys.*, **21**, 2363–2381, https://doi.org/10.5194/acp-21-2363-2021.